Design of a Cryogenic RF Coil Prototype for a Full Body 1.5T MRI Receive Array

Zhurbenko, Vitaliy; Gosselink, Mark ; Voogt, Ingmar ; Alborahal, Cezar ; Hoogduin, Hans ; Jepsen, Rasmus Alexander ; Sanchez Heredia, Juan Diego; Klomp, Dennis

Published in:
Proceedings of the 2024 ISMRM

Publication date:
2024

Document Version
Peer reviewed version

Design of a Cryogenic RF Coil Prototype for a Full Body 1.5T MRI Receive Array

Vitaliy Zhurbenko[1], Mark Gosselink[2], Ingmar Voogt[3], Cezar Alborahal[2], Hans Hoogduin[2], Rasmus Alexander Jepsen[1], Juan Diego Sanchez Heredia[1], Dennis Klomp[2]
[1]Technical University of Denmark, Denmark
[2]University Medical Center Utrecht, The Netherlands
[3]WaveTronica B.V., The Netherlands

Introduction:

An RF coil is the first component in the MRI scanner receiver chain. This component therefore defines signal-to-noise ratio (SNR) and influences image quality. The ultimate goal of MRI development has always been to increase SNR. As the name indicates, SNR increase can be achieved by increasing the signal level and by decreasing the noise. The majority of efforts in the history of MRI development have been focused on increasing the signal. This is the reason typical MRI scans often rely on close-fitting coils. From a usability perspective and for the comfort of the patient it is beneficial to eliminate close-fitting RF coils[1] and make them virtually invisible by integrating them into the scanner bore. In this work, this approach is studied, and a prototype of an integrated coil is developed.

Methods:

Placing RF coils further away from the patient reduces the received signal. To maintain SNR, the noise should be decreased accordingly. Apart from interference, there are two sources of noise in the receive coil. Intrinsic noise of the coil and the noise coming from the patient. The coil thermal noise can be reduced by cryogenic cooling, while patient noise can be reduced by shrinking the field of view. To recover the original field of view, the number of coils is increased forming an array of receive elements. The receive array can be shaped as a large cylinder conforming to the bore, as conceptually illustrated in Fig. 1, and complement a standard transmitting birdcage coil (not shown). Fig.1 also shows the resulting B_1^- field in one row of coils simulated with CST.
To test the concept, one element of such a receive array is designed and constructed.

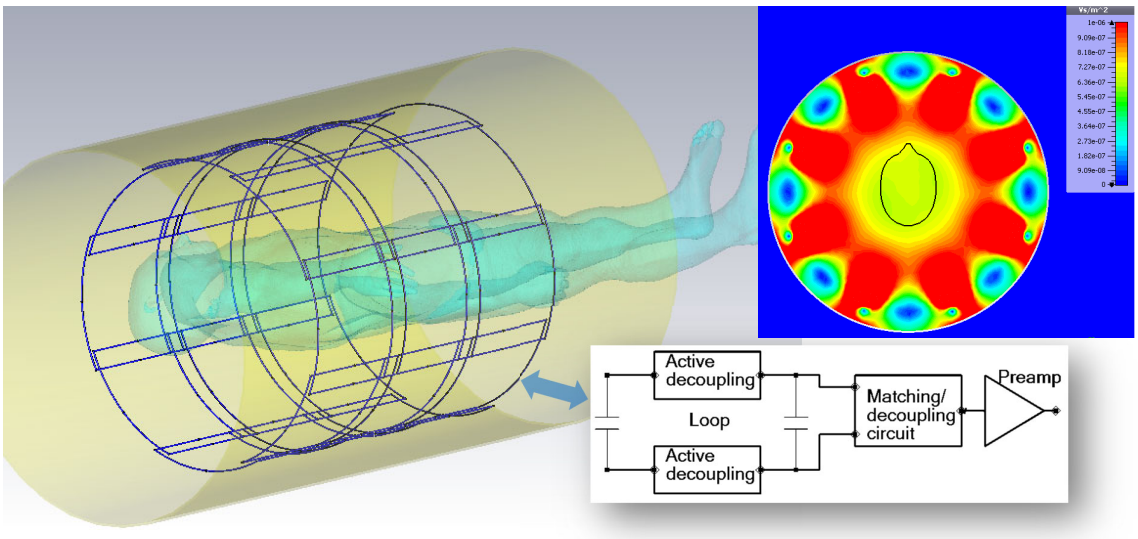

Fig. 1. Sketch of a wide bore receive array and a block diagram of each element. Simulated B_1^- normalized to 1W accepted power for one row of 8 elements.

The receiving element is placed very close to the transmitting birdcage coil[2], which requires a reliable decoupling strategy. Two active decoupling circuits on the loop and a preamplifier decoupling circuit are used, as shown on the element block-diagram in Fig.1. The corresponding circuit diagram and simulation setup are shown in Fig.2.

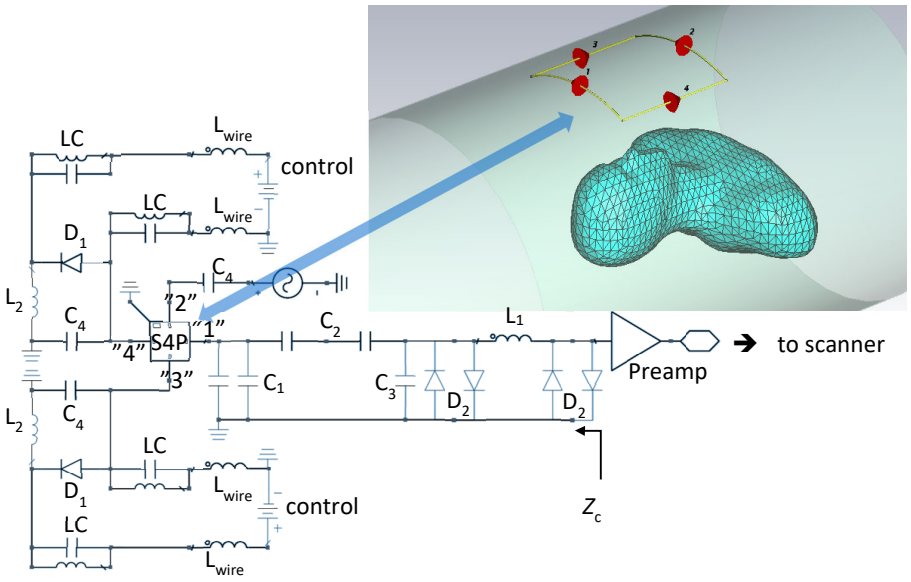

Fig. 2. Circuit electromagnetic co-simulation. C1, C2, and C3 form a Pi matching/decoupling network. L1 is a preamplifier impedance extension element. C4 denotes coil segmenting capacitors. L2 designates active decoupling blocking components. D1 refers to PIN diode switching elements. LC is tuned to the 1H Larmor frequency and feeds the active decoupling control signal. L_{wire} models reactances of the connection wires. D2 indicates protection cross diodes. The AC signal source models received MR signal.

The field in the loop is analyzed with CST frequency domain solver using adaptive tetrahedral mesh refinement and a Virtual Family Duke v2 shell phantom[3, 4]. The corresponding scattering matrix is imported into Keysight ADS for circuit analysis. The preamplifier decoupling network is a three-element Pi network, which is based on the concept described in [5] and using design equations from [6, 7]. The impedance of the preamplifier is extended with the reactance of L_1. The preamplifier is ElCry2-u[8] modified for cryogenic operation and noise pre-matched to 50Ω at ~63.9MHz using equations from [6, 7].

The coil is fabricated according to the design in Fig.2. The loop size is ~26cm x 27cm in the *z*- and *x*-directions correspondingly. It is constructed of the copper outer conductor of a .141CU-C-L-50 coaxial cable (3.58mm outer diameter). The coil holder was 3D printed. A photograph of the coil with the upper cover removed is shown in Fig.3(a).

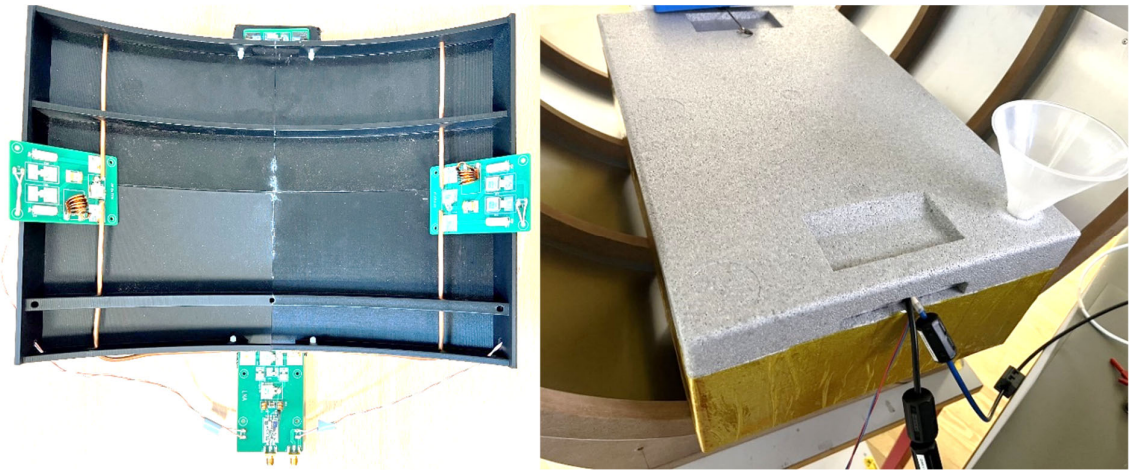

(a) (b)

Fig. 3. (a) Photograph of the cryogenic coil prototype with the upper cover removed. (b) Coil in a thermal box during cryogenic testing.

Results:

The impedance of the coil at the preamplifier terminals at room temperature as measured by a network analyzer was $Zc \approx 42\Omega$ (see Fig.2).

For the analysis, it is assumed that the copper conductivity increases from $5.8 \cdot 10^7$ S/m to $2.86 \cdot 10^8$ S/m at 77K[9]. The loop wire resistivity and the loss of the implemented lumped components is assumed to decrease accordingly with a factor of ~4.9. The results of the preamplifier decoupling and SNR analysis are shown in Fig. 4.

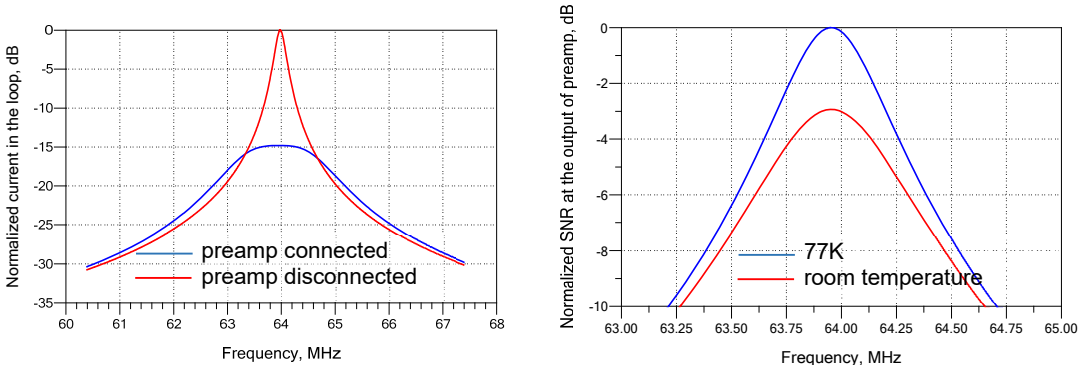

(a) (b)

Measured Q-factor at room temperature	
Unloaded	160
Loaded	130

(c)

Fig. 4. (a) Simulated current in the loaded loop at room temperature with and without preamplifier connected illustrating preamplifier decoupling; (b) simulated normalized SNR sweep at the output of the preamplifier when loop wires and circuit components are cooled. Preamplifier noise figure change due to cooling is not considered due to model limitations. (c) Measured Q-factor of the loop with preamplifier disconnected. Human head loading.

Discussion and Conclusion:

As expected, preamplifier decoupling decreases the signal current in the loop due to spoiling the coil resonator Q-factor. The decrease is about 15dB due to a high reflection coefficient at

the coil terminals compared to the resonant case. Preamplifier decoupling, however, does not affect the SNR, since, along with the signal, the coil noise is also reflected, which maintains the overall sensitivity. Though the preamplifier decoupling is lower than one would typically expect from alternative room temperature commercially available preamplifiers. This is mainly due to the implemented preamplifier having additional integrated high-power protection circuits, since it is placed very close to the transmitter.
The SNR improvement due to cooling is expected to be in the range of 3dB. This does not account for any preamplifier noise figure change due to cooling. The coil is currently being tested and the imaging results can be found in the slideshow on the conference website.

References:

1. Sodickson, D.K., Zhang, B., Duan, Q., et al. Is a 'one size fits all' many-element bore-lining remote body array feasible for routine imaging? Proc. Int. Soc. Magn. Reson. Med. 2014, 22, 618.
2. Branderhorst W., Steensma B., Beijst C., et al. Evaluation of the radiofrequency performance of a wide-bore 1.5 T positron emission tomography/magnetic resonance imaging body coil for radiotherapy planning. Physics and Imaging in Radiation Oncology. 17 (2021) 13–19.
3. Andreasen H.K. Design and Implementation of an 8-channel Array for High Field MRI. Bachelor's thesis. Electromagnetic Systems, Department of Electrical Engineering. DTU, Ørsteds Plads, Building 348, 2800 Kgs. Lyngby Denmark. 2021.
4. Gosselin M-C., Neufeld E., Moser H., et al. Development of a new generation of high-resolution anatomical models for medical device evaluation: the Virtual Population 3.0. Physics in Medicine & Biology. 2014;59(18):5287.
5. Roemer P. B., Edelstein W. A., Hayes C. E., et al. The NMR phased array. Magnetic Resonance in Medicine. 1990;16(2):192-225.
6. Wang W., Zhurbenko V., Sanchez-Heredia J.D., Ardenkjær-Larsen J. H. Three-element matching networks for receive-only MRI coil decoupling. Magnetic Resonance in Medicine. 2021;85(1):544-550.
7. Wang W., Zhurbenko V., Sanchez-Heredia J. D., Ardenkjær-Larsen J. H. Trade-off between preamplifier noise figure and decoupling in MRI detectors. Magnetic Resonance in Medicine. 2023;89(2):859-871.
8. ElCry. Ultra-Wideband Low-Noise Preamplifier ElCry2-u. http://elcry.com/vz/elcry2-u.pdf. Accessed: 2023-07-21.
9. Cryogenic Properties of Copper. https://www.copper.org/resources/properties/cryogenic/. Accessed: 2023-07-21

Acknowledgement: The authors would like to thank Jóan Hofgaard Køtlum for PCB layout and fabrication as well as Innovation Fund Denmark for partial support under E2409 grant.